# The Seismic Record
# FAULT SLIP POTENTIAL NEAR THE DEADLY MW6.8 OUKAÏMEDENE, MOROCCO EARTHQUAKE
## --Manuscript Draft--

| | |
|---|---|
| **Manuscript Number:** | |
| **Full Title:** | FAULT SLIP POTENTIAL NEAR THE DEADLY MW6.8 OUKAÏMEDENE, MOROCCO EARTHQUAKE |
| **Article Type:** | Research Article |
| **Corresponding Author:** | Will Levandowski<br>Tetra Tech, Inc.<br>Chapel Hill, NC UNITED STATES |
| **Corresponding Author's Institution:** | Tetra Tech, Inc. |
| **First Author:** | Will Levandowski |
| **Order of Authors:** | Will Levandowski |
| **Manuscript Region of Origin:** | UNITED STATES |
| **Abstract:** | Thousands were killed by the September 8, 2023, Mw6.8 Oukaïmedene, Morocco earthquake in the Western High Atlas. To determine the fault orientations most likely to host aftershocks and future large earthquakes, the regional crustal stress field is estimated from inversions of focal mechanisms from the High/Middle Atlas junction area, Central, and Western High Atlas., and the associated fault slip potential is modeled. North-south shortening is accommodated by roughly equal parts reverse and strike-slip motion. As such, many fault orientations are optimally aligned for slip: steep NE-, SW-, SSE-, or NNW-striking planes, gently (~25°) dipping east- and west-striking planes, and orientations between. Aftershocks are most likely to be triggered on these faults, while steep E–W and nearly all N–S faults are relatively more stable. |
| **Suggested Reviewers:** | Fida Medina<br>f_medina@geoscimar.org<br>Expert in Atlas area focal mechanisms |
| | Gavin Hayes<br>ghayes@usgs.gov<br>Expert in finite-fault models |
| | Roger Bilham<br>bilham@colorado.edu<br>Expert in earthquake source processes and tectonics |
| | Jens-Erik Lundstern<br>jlundsnee@usgs.gov<br>Expert in stress inversions and fault slip |
| **Opposed Reviewers:** | |

**TETRA TECH**

Dear Editor—

Please consider the submission "Fault slip potential near the deadly $M_w$6.8 Oukaïmedene, Morocco earthquake" for publication in TSR. The manuscript presents stress inversions and geomechanical calculations aiming to determine what fault orientations are most likely to experience aftershocks and future ruptures.

The article is certainly timely and will hopefully be of interest to TSR readers and the seismological community. Thank you for your consideration.

Best wishes,

Will Levandowski
will.levandowski@tetratech.com
Senior Geophysicist
Tetra Tech, Inc.
Chapel Hill, NC
09/15/2023

1    **FAULT SLIP POTENTIAL NEAR THE DEADLY Mw6.8 OUKAÏMEDENE, MOROCCO EARTHQUAKE**

2    Will Levandowski, Tetra Tech, Inc.

3    Will.Levandowski@tetratech.com

4

5    **Abstract**

6    Thousands were killed by the September 8, 2023, Mw6.8 Oukaïmedene, Morocco earthquake in the Western High

7    Atlas. To determine the fault orientations most likely to host aftershocks and future large earthquakes, the

8    regional crustal stress field is estimated by inverting focal mechanisms from the High/Middle Atlas junction area,

9    Central, and Western High Atlas, and the associated fault slip potential is modeled. North-south shortening is

10   accommodated by roughly equal parts reverse and strike-slip motion. As such, many fault orientations are

11   optimally aligned for slip: steep NE-, SW-, SSE-, or NNW-striking planes, gently (~15–40°) dipping east- and

12   west-striking planes, and orientations between. Aftershocks are most likely to be triggered on these faults, while

13   steep E–W and nearly all N–S faults are relatively more stable.

14

15   **Introduction**

16          Rapidly characterizing the stress field and locally favorable fault orientations may identify faults that are

17   most likely to host aftershocks during an ongoing seismic sequence.  An investigation of the crustal stress field

18   near the epicenter of the 8 September 2023 Mw6.8 Oukaïmedene, Morocco earthquake (**Figure 1**) and associated

19   fault slip potential (FSP) models are presented here. Crustal stress is determined by inversions of earthquake focal

20   mechanisms from the western to central High Atlas and the High/Middle Atlas junction (**Figure 2**). The resulting

21   stress tensors are input to FSP models, which quantify the suitability for slip in the local stress field as a function

22   of fault orientation. These quantifications should identify the fault orientations most likely to host aftershocks in

23   the coming days to weeks, as well as future mainshocks.

24          With nearly 3,000 people already known to have died, the Mw6.8 earthquake is the deadliest in Morocco

25   since the 1960 M5.9 in Agadir (**Figure 2**). Moment tensors from the USGS NEIC and Quick CMT indicate

moderately steep WSW- and gently dipping ESE-striking nodal planes (N255E, 69°–73° and N122E, 29°: see

Data and Resources). These planes were used by USGS in finite-fault models jointly constrained by InSAR and

teleseismic waveforms (see Data and Resources). Hypocentral depths range from 26 to 33 km across these

models.
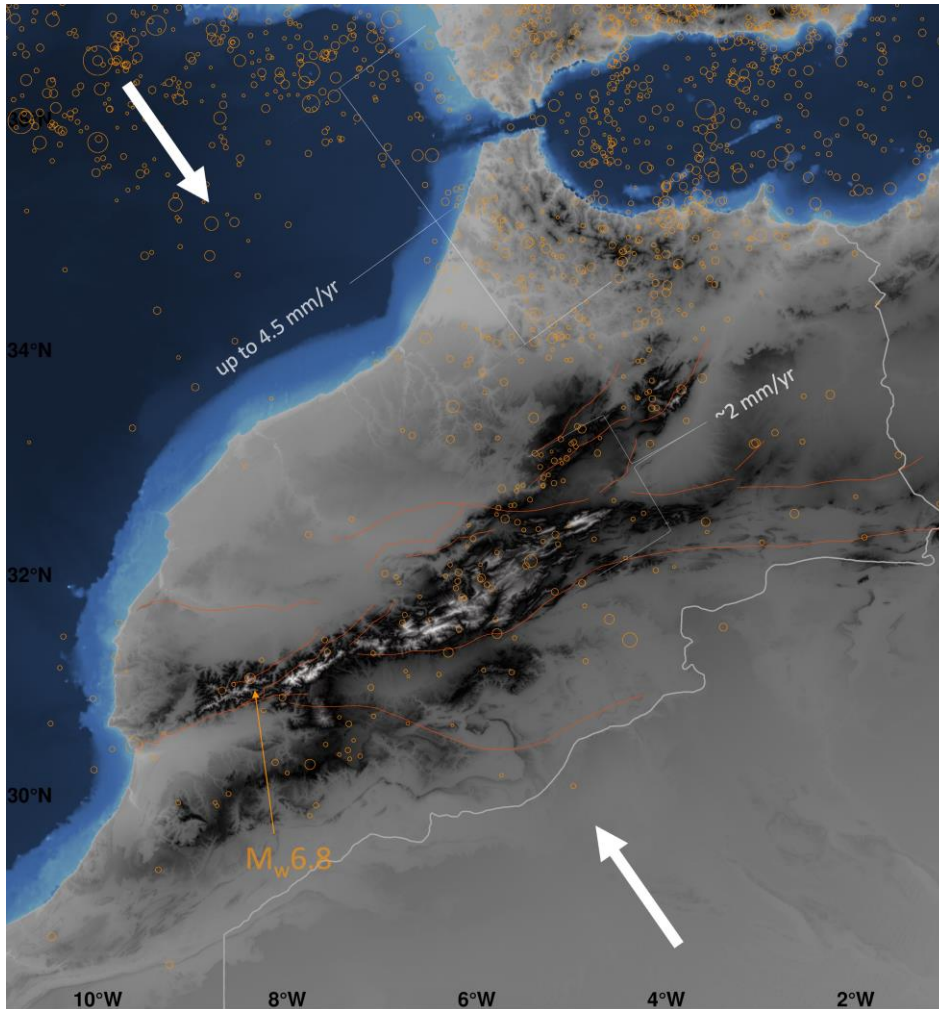


**Figure 1: Overview** of regional tectonics. Red-orange lines: Major faults within the main study region digitized from El

Moudnib et al. (2023). Orange circles: Seismicity 1522–2005 (Peláez et al., 2007). White arrows show convergence direction.

## Setting

Morocco marks the SW corner of the vast Alpine-Himalayan orogen, and strain in the High Atlas marks the southernmost extent of this shortening. As the African plate converges obliquely NNW with the Eurasian plate, some 4.5 mm/yr of shortening are absorbed by the Rif Mountains in northernmost Morocco and Algeria. Meanwhile 2 mm/yr are transmitted ~500 km south of the plate boundary to the Atlas Mountains system (Azzouzi et al. 2005).

From north to south, the Atlasic domains comprise the NE-trending Middle Atlas, E-trending eastern High Atlas, ENE-trending central High Atlas, and NE-trending western High Atlas, all of which are bounded by locally range-parallel thrust faults (**Figure 1**). From the central High Atlas (e.g., High/Middle Atlas junction) to the western High Atlas, including near the epicenter, these thrusts rotate from nearly perpendicular to shortening to oblique to shortening. As a result, deformation appears to transition from dominantly reverse faulting with a minor strike-slip component in the more seismically active High-Middle Atlas junction (El Moudnib et al., 2023) to oblique faulting near the epicenter and westward through Agadir (**Figure 2**).
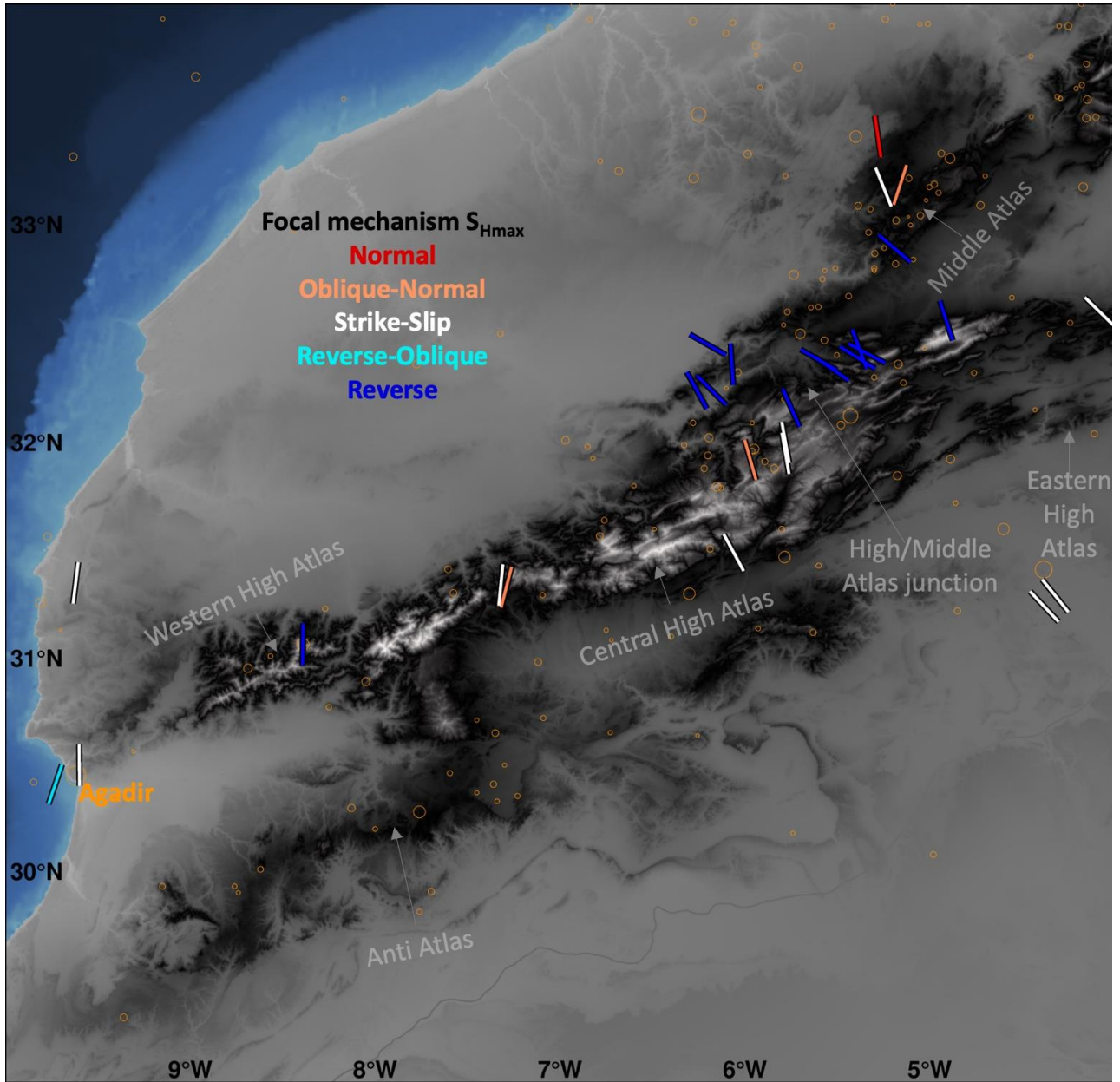
55 **Figure 2: Focal mechanisms** within the study area depicted as bars oriented in the maximum horizontal shortening direction

56 and color-coded by faulting style (following the convention of Zoback, 1992).

57

58 **Crustal Stress**

59 *Previous Work and Data*

60     Focal mechanisms have been compiled by Medina (2008) for all of Morocco and more recently by El

61 Moudnib et al. (2023) for the High/Middle Atlas Junction area. Hatzfeld et al. (1977) provided a solution for the

62   1960 Agadir earthquake. Several events have moment tensors available from the global CMT project, GFZ-

63   Geofon, USGS, and INGV. No additional data are available from the World Stress Map (Heidbach et al., 2016).

64        With sparse historical to instrumental seismicity in the epicentral, a rather expansive region (**Figure 2**)

65   from -10° to -4° longitude and 28° to 34° latitude is examined (data from farther west and south would be

66   included, but none were found), availing focal mechanisms for 28 earthquakes. With caution that a single focal

67   mechanism—or even a few—does not constrain the local stress tensor (e.g., McKenzie, 1969), these display some

68   coherent geographic patterns. All have NW- to N-trending maximum shortening directions $S_{Hmax}$ (the P-axis for

69   reverse to strike-slip events), consistent with regional strain. In the Central and Western High Atlas, strike-slip

70   faulting is dominant, and P-axes trend approximately north. Reverse faulting mechanisms with NW-trending P-

71   axes typify the High/Middle Atlas junction area. Three mechanisms in the Middle Atlas display a variety of

72   faulting styles and $S_{Hmax}$, while three mechanisms from the Eastern High Atlas and south have strike-slip

73   mechanisms with NW-trending P-axes. These latter two may reflect different states of stress from that near

74   Oukaïmedene and are thus preferably omitted from the analysis.

75        El Moudnib et al. (2023) derived 15 focal mechanisms near the High/Middle Atlas junction, which they

76   combined with several others from the southern Middle Atlas, Eastern and Central High Atlas, and areas to the

77   southeast in a single stress inversion. The best-fit tensor favors nearly pure reverse faulting with N–S shortening

78   (the Aϕ parameter described below equals 2.5±0.1, with $S_{Hmax}$ N2E). The present analysis focuses on the Western

79   High Atlas, some 300 km southwest of El Moudnib et al.'s focus, and includes four additional mechanisms from

80   that area.

81

82   *Stress Inversions*

83        Inversions of focal mechanisms are well established and stem from the axiom that coseismic slip parallels

84   the shear traction resolved on the fault plane (e.g., Angelier, 1979). The latter depends linearly on fault orientation

85   and the 3D stress tensor. Under the condition that the selected earthquakes all occurred under the same stress

86   field, this linear system quickly becomes overdetermined with multiple slip observations from faults of different

87   orientations. Inverting this linear system solves for the 3D stress tensor that minimizes the angular misfit between

88  the slip vectors and shear traction on the respective fault planes. By convention, 20 or more focal mechanisms are

89  needed for reliable stress inversions (e.g., Townend and Zoback, 2004).

90  The normalized stress tensor can be fully described in terms of the directions and ratio of magnitudes of

91  the principal stresses $\phi$:

92  $$\phi = (S_2 - S_3) / (S_1 - S_3) \tag{1}$$

93

94  with $S_1$ the magnitude of the maximally compressive stress, $S_2$ intermediate, and $S_3$ the minimum.

95  Simpson (1997) combined $\phi$ with the style of faulting (normal/strike-slip/reverse, as defined by principal

96  axis plunges; Zoback, 1992) to describe the style of deformation as a quantity $A\Phi$:

97

98  $$A\Phi = (n + 0.5) + (-1)^n(\phi - 0.5) \tag{2}$$

99

100  In equation 2, $n$=0 for normal faulting, 1 for strike-slip, and 2 for thrust. Consequently, $A\Phi$ defines a continuum

101  from radial extension ($A\Phi = 0$) to radial contraction ($A\Phi = 3$), passing through: uniaxial extension/pure normal

102  faulting ($A\Phi$=0.5); oblique extension ($A\Phi$=1.0); horizontal shear/strike-slip ($A\Phi$=1.5); oblique contraction

103  ($A\Phi$=2.0), and uniaxial contraction/pure reverse faulting, ($A\Phi$=2.5).

104  The inversion algorithm (following Levandowski et al., 2018a) aseesess uncertainty with 1001 Monte

105  Carlo realizations. Each realization jackknife-resamples the dataset (discarding $n_{mechanisms}^{0.5}$), randomly perturbs

106  the individual slip vectors by ±15° and chooses a random coefficient of friction between 0.3 and 0.9. The retained

107  mechanisms are then iteratively inverted (following Vavryčuk, 2014), selecting the less stable of the two nodal

108  planes for each event with respect to the current estimate of the stress tensor, inverting these mechanisms for an

109  updated stress estimate, and recomputing the stability of each plane, for a total of 5 iterations per realization. A

110  total of 1001 realizations are used for the inversion, and the values discussed are the median ± one standard

111  deviation.

112  The preferred set of mechanisms is geographically limited to the High/Middle Atlas junction, Central and

113  Western High Atlas (south of 32.75° latitude and west of -4.5° longitude) and comprises 21 mechanisms (**Figure**

114 **S1**). In the preferred approach, the individual mechanisms are weighted by inverse-distance from the M6.8

115 epicenter. Inversions under nine different parameterizations are summarized in **Table S1** (Models 0–8): Results

116 are relatively insensitive to the inversion setup. Details of the focal mechanisms are provided in **Table S2**.

117 Inverting the preferred set yields a reverse-oblique faulting regime (AΦ=2.07±0.15) that accommodates

118 north-south horizontal shortening N2E (±5°) (**Figure 3**). Fit to the mechanisms is acceptable, with average

119 angular misfit 25.5° between the shear traction on each respective focal plane and the slip vector on the iteratively

120 selected focal plane. A value of 40–45° is often taken as a threshold for homogenous stress (Michael et al., 1990;

121 Michael, 1991). By contrast, the auxiliary planes mismatch by an average of 43°.

122



Oukaimedene: Oblique shortening
$A\phi=2.07\pm0.15$
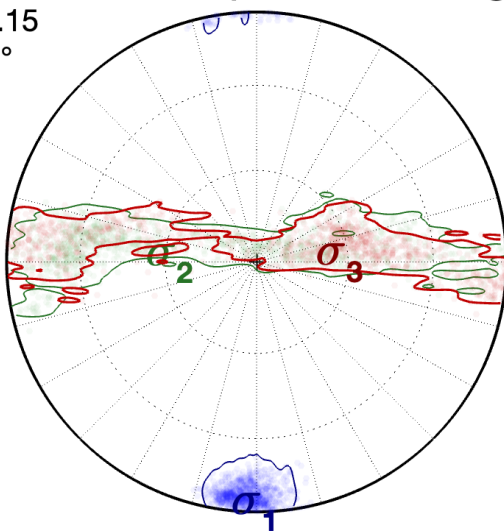$\sigma_{Hmax}$N2E±5°
n=21

**Figure 3: Stress inversion results** Lower hemisphere projection of principal stress axes from 1001 inversions. The maximum compressive stress in the western High Atlas and environs is horizontal and north/south. The other two stresses (horizontal, east/west and sub-vertical) are approximately equal in magnitude. This stress promotes north-south shortening by a nearly even mix of reverse and strike-slip

134 faulting.

135

136

137

138 **Fault Slip Potential Modeling**

139 FSP modeling provides a quantitative metric for how well faults are oriented for frictional slip in the local

140 stress field. From the normalized stress tensors derived from focal mechanism inversions, the full stress tensors

141 are calculated (following Walsh and Zoback, 2016; Levandowski et al., 2018b) at a nominal depth, here 5 km.

142 The shear and normal tractions are computed as functions of fault orientation (strike and dip), and the suitability

143 of faults for slip is then quantified in terms of distance from Coulomb failure, or the difference between the

144 computed shear traction magnitude and the frictional resistance:

145

146 $$dCFS = \text{friction x } |\text{effective normal traction}| - |\text{shear traction}| \qquad (3)$$

147

148 Thus, dCFS represents the shear stress increase that may trigger slip on a pre-existing fault. The

149 underlying assumption of FSP modeling is that the crust is in a state of frictional failure equilibrium (e.g., Zoback,

150 2010), meaning that at least one fault in the local stress field has dCFS = 0 MPa.

151 Because FSP under a given stress depends only on the fault strike and dip, it provides a complementary

152 constraint to stress inversions, which treat strike and dip as fixed and minimize misfit to slip vectors (rake). This

153 combination can be also used to disambiguate the focal and auxiliary planes and choose from different focal

154 mechanism solutions for a single event (Levandowski et al., 2023).

155 The Monte Carlo-style stress inversions provide 1001 estimates of the normalized stress tensor. Each of

156 these 1001 models and its attendant friction are used to compute the full stress tensor and then the shear and

157 normal tractions and dCFS for all possible fault planes (following the approach of Levandowski et al., 2018b;

158 2023). Overburden density is varied randomly across the 1001 realizations from 2650 to 2850 kg/m$^3$. Pore

159 pressure is set to hydrostatic. The values of dCFS discussed here are the 95% confidence lower bound: in 5% of

160 Monte Carlo trials, this increase in CFS (or less) would trigger instability on the fault plane in question.

161    This 95% confidence lower bound averages 2.8 MPa on the iteratively selected focal planes (**Figure 4**,
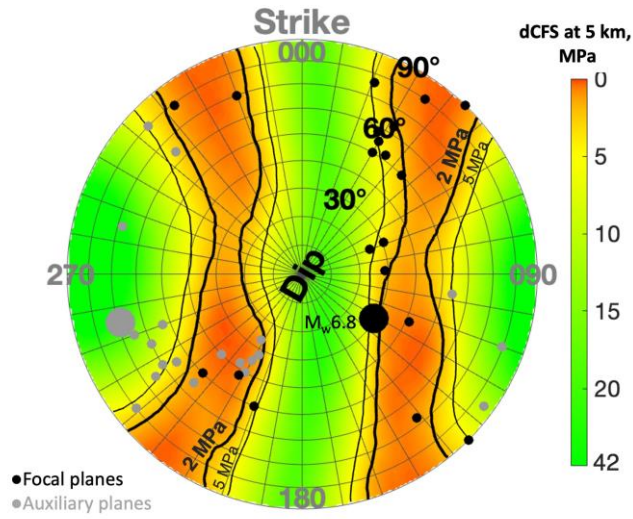
162    black dots). For comparison, in cases of induced seismicity, most events are retrospectively found to have occurred on faults within ~2 MPa of failure (also for a nominal depth of 5 km; Walsh & Zoback, 2016). The auxiliary planes are comparatively far from failure, with average 95% confidence dCFS of 7.1 MPa (**Figure 4**, gray dots).



172    **Figure 4: Fault slip potential** quantified in terms of dCFS (Coulomb stress change to instability, Equation 3). The values

173    shown are the 95% lower confidence bound across 1001 inversions for faults oriented as described by the strike and dip polar

174    axes. The iteratively selected focal planes for the best-fit stress are shown as black dots. Their auxiliary planes are shown as

175    gray dots. Large dots denote the Oukaïmedene earthquake. The ESE-striking, gently dipping nodal plane is well aligned in the

176    regional stress field (dCFS=3.6 MPa), while the N255E plane appears poorly oriented (dCFS=22.6 MPa).

177

178

179

180    **Results**

181    In regions with mixed modes of faulting, many fault orientations are potentially active (Levandowski et

182    al., 2018b). The ~N–S oblique shortening in the western High Atlas can be accomplished by strike-slip on steep

183    faults striking NE, SW, SSE, or NNW, by reverse motion on gently (~30°) dipping faults striking east/west, or by

184    oblique slip on orientations between these (**Figure 4**). High FSP (low dCFS) faults thus form two continua rather

185    than two (reverse and normal) or four (strike-slip) isolated optimal orientations.

186    This diversity notwithstanding, many orientations are not favorable for slip, including NNW–SSE faults

187    of any dip and E–W faults any steeper than ~50°. Indeed, the iterative focal/auxiliary plane determination

188    (Vavryčuk, 2014) does not select a steep E–W fault for any of the events.

189    Seismic moment tensors of the $M_w6.8$ feature a gently dipping ESE-striking plane well oriented for

190    reverse-oblique faulting under north-south shortening and a WSW-striking fault that is quite steep (dip 69°)

191    relative to the maximum stress vector derived here. Indeed, the N255E plane (large gray dot in **Figure 4**) is at

192    least 21.9 MPa from failure in 95% of the models while its N122E complement (large black dot in **Figure 4**) may

193    be within 3.6 MPa (**Figure 5**). Given only these two choices, stress considerations favor the ESE-striking plane as

194    the causative fault.
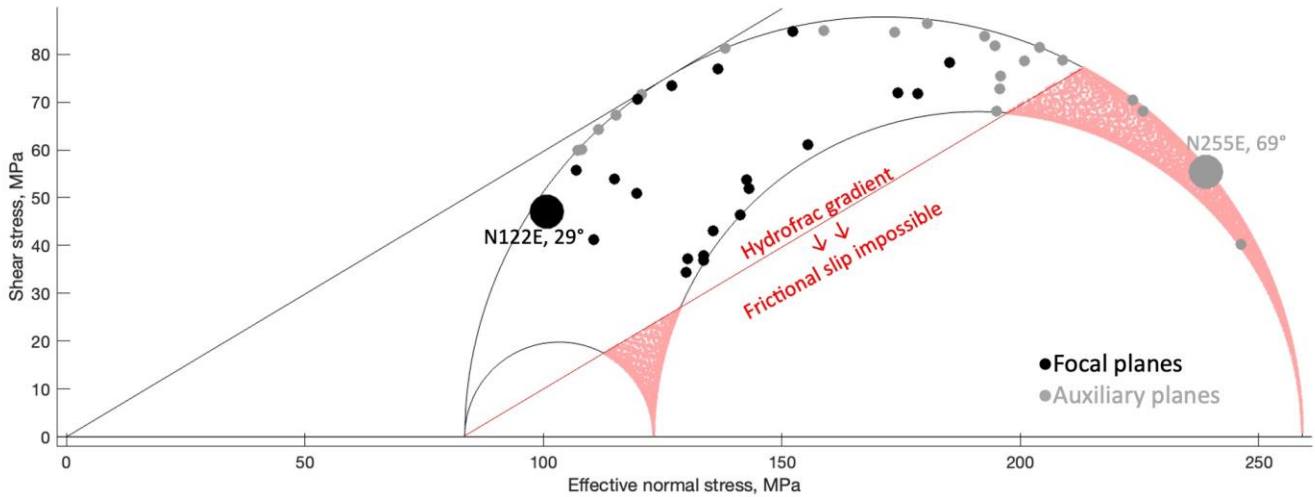
195



196

197    **Figure 5: Mohr Circle** for the single best-fit stress tensor under the preferred inversion scheme. Red indicates the area

198    beyond the hydrofracture gradient, which is incompatible with frictional slip. The ESE-striking nodal plane (large black dot) is

199    well aligned for slip, while the WSW-striking plane lies beyond the hydrofracture gradient for this specific stress tensor. Note

200    that 1001 tensors were developed under this inversion setup, and this plane is not slip-incompatible in all models under this or

201    other parameterizations (see Table S1).

202

203    This finding contrasts with the finite fault model developed jointly from InSAR and seismic waveforms

204    (see Data and Resources) in which the WSW-striking plane provides superior fit, especially to surface waves

205 (Yeck, written communication 2023– see Acknowledgements). To determine whether other parameterizations or

206 focal mechanism groupings would favor this plane, a variety of additional cases were considered (**Table S1**).

207 These include imposing low-friction faults (**Figure S2**), allowing only the SW-striking nodal planes to be selected

208 (**Figure S3**), and both. Still, the ESE nodal plane remains closer to failure (dCFS = 2.2 MPa) than the WSW plane

209 (5.5 MPa) (**Figure S4**). It is important to note that the finite-fault model is sensitive to the slip realized during the

210 earthquake, while the stress estimates most specifically pertain to rupture nucleation.

211     The major, active range-bounding faults mostly strike SW to WSW. Indeed, **Figure 4** indicates that

212 WSW-striking faults with ~15–40° dips may be optimally oriented, while SW-striking faults with dips anywhere

213 from ~20° to 90° could be optimally aligned. The regional fault system comprises numerous sub-parallel strands

214 (**Figure 1**), presumably with varying dips and variable dip with depth. Rupture nucleation would be most likely

215 on a patch with favorable orientation—either a gentler WSW- or similarly steep SW-striking fault— but could

216 have propagated up-dip onto steeper sections or laterally onto more westerly segments (Goldberg, written

217 communication 2023– see Acknowledgements). Thus, the discrepancy does not impugn the finite-fault model or

218 moment tensors but rather presents the possibility that slip occurred on a curved surface or multiple neighboring

219 patches.

220     A second possibility is that stress differs in the Western High Atlas from areas farther east, where most of

221 the available data comes from. This local stress may not be adequately modeled because of the paucity of data

222 near Oukaïmedene. Inversions were conducted (Models 9–11, **Table S1, Figure S1**) for progressively smaller

223 areas around the epicenter, although with fewer mechanisms—n=15, 10, and 6—than needed for a reliable result.

224 Doing so (**Figure S5**) progressively decreases $A\phi$ and increases the slip potential of the WSW nodal plane. At the

225 extreme, with only the 6 mechanisms from the Western High Atlas (Model 11), the median stress regime

226 approaches pure strike-slip, $A\phi=1.59\pm0.24$, and the two nodal planes are approximately equally likely to slip.

227 Thus, with insufficient data, it remains permissible that the stress regime in the Western High Atlas transitions to

228 favor strike-slip more heavily and thus allows reactivation of a moderately steep WSW-striking nodal plane.

229

230

231

**Conclusions**

The crustal stress field across the Central and Western High Atlas is characterized by north–south

maximal compression and favors a mix of reverse, reverse-oblique, and strike-slip faulting. Several fault

orientations are well oriented for slip in the modern stress field (**Figure 4**) and are thus likely to host aftershocks

or future ruptures: east-west reverse faults dipping ~15-40°, steep NE–SW or SSE–NNW strike-slip faults, and

reverse-oblique faults between these orientations. By contrast, east-west planes dipping more than ~50° and

nearly all north-south faults appear unlikely to slip.

Moment tensor nodal planes from the $M_w$6.8 Oukaïmedene earthquake are oriented N122E, 29° and

N255E, 69°. Fault slip potential calculations find the latter to be too steep (or too westerly) to be well-aligned for

slip, yet a finite fault model finds significantly better fit to waveforms and InSAR with this plane than the former.

Further, the regional range-bounding fault network comprises multiple sub-parallel SW- to WSW-striking strands.

The slip potential models indicate that WSW-striking faults dipping ~15–40° and SW–striking faults of nearly

any dip may be optimally oriented. Thus, it is plausible that rupture nucleated on a less steep or more

southwesterly patch within thrust fault network and propagated onto the segment identified by moment tensors

and the finite fault model. A second possibility is that stress in the Western High Atlas differs from areas farther

east, where most of the available focal mechanisms are. Western High Atlas data are limited to six mechanisms,

and inverting these permits that strike-slip faulting becomes dominant such that the ESE plane and steeper WSW

plane are equally likely to rupture. Inversions with so few data are not reliable, however, so ongoing studies of

surface deformation, aftershock distribution, and focal mechanisms will be needed to resolve local stress in the

Western High Atlas.

255

## Data and Resources

Focal mechanism details are provided in Table S2 and are available in the referenced literature. Oukaïmedene moment tensors from (https://earthquake.usgs.gov/earthquakes/eventpage/us7000kufc/moment-tensor, last accessed 12 September 2023) and Global CMT (https://www.globalcmt.org/CMTsearch.html, last accessed 11 September 2023) (Dziewonski et al., 1981; Ekstrom et al., 2012). Finite fault model from (https://earthquake.usgs.gov/earthquakes/eventpage/us7000kufc/finite-fault, last accessed September 14, 2023). Stress inversion and FSP codes are available at github.com/WillLevandowski/

## Declaration of competing interests

The author declares no competing interests.

## References

Angelier, J. (1979) Determination of the mean principal stresses for a given fault population, Tectonophysics 56, T17-T26, 1979.

Angelier, J. (1990) Inversion of field data in fault tectonics to obtain the regional stress, III, A new rapid direct inversion method by analytical means, GeophysJ. . Int., 103, 363-376, 1990.

Azzouzi, R., M. Ettarid, H. Semlali, A. Rimi, A. Trache, M. Aït Belaid, and L. Aït Brahim (2005). Actual horizontal displacements and parametric deformation determinations of African and Eurasian tectonic plates in the Western Mediterranean region. Workshop on Fracture Dynamics: Theory and Applications to Earthquakes.

Dziewonski, A. M., T.-A. Chou and J. H. Woodhouse (1981) Determination of earthquake source parameters from waveform data for studies of global and regional seismicity, J. Geophys. Res., 86, 2825-2852. doi:10.1029/JB086iB04p02825

279    El Moudnib, L., Timoulali, Y., Nouayti, A., El Abbassi, M., Bouka, M., Nouayti, N., & Mhammdi, N. (2023).

280          Seismotectonic model of High-Middle Atlas Junction (Morocco) derived from earthquake focal

281          mechanism and stress tensor analysis. *Modeling Earth Systems and Environment*, *9*(2), 2407-2423.

282    Ekström, G., M. Nettles, and A. M. Dziewonski (2012) The global CMT project 2004-2010: Centroid-moment

283          tensors for 13,017 earthquakes, Phys. Earth Planet. Inter., 200-201, 1-9, doi:10.1016/j.pepi.2012.04.002

284    Hatzfeld D., Frogneux M. & Girardin N. 1977. Etude de la sismicité dans la région de l'arc de Gibraltar et

285          l'Algérie du Nord. Bull. Soc. Géol. Fr., (7), XIX, n°4, 741-747.

286    Heidbach, O., M. Rajabi, X. Cui, K. Fuchs, B. Müller, J. Reinecker, K. Reiter, M. Tingay, F. Wenzel, F. Xie, M.

287          O. Ziegler, M.-L. Zoback, and M. D. Zoback (2018): The World Stress Map database release 2016:

288          Crustal stress pattern across scales. Tectonophysics, 744, 484-498, doi:10.1016/j.tecto.2018.07.007

289          Heidbach, Oliver; Rajabi, Mojtaba; Reiter, Karsten; Ziegler, Moritz, WSM Team (2016): World Stress

290          Map Database Release 2016. GFZ Data Services, doi:10.5880/WSM.2016.00

291    Levandowski, W., Weingarten, M., and Walsh F.R. III. (2018) Geomechanical sensitivities of injection-induced

292          earthquakes: *Geophysical Research Letters*, v. 45, doi:10.1029/2018GL077551

293    Levandowski, W., Herrmann, R.B., Briggs, R., Boyd, O.S., and Gold, R. (2018) A revised stress map of the

294          continental United States reveals evidence for heterogeneous intraplate stress: *Nature Geoscience*, v. 11,

295          doi:10.1038/s41561-018-0120-x.

296    Levandowski, W., C. Powell, M. Chapman, and Q. Wu (2023). Anomalous Crustal Stress in the Eastern

297          Tennessee Seismic Zone, Seismol. Res. Lett. XX, 1–13, doi: 10.1785/0220220364.

298    Michael, A. J., Ellsworth, W. L., & Oppenheimer, D. H. (1990). Coseismic stress changes induced by the 1989

299          Loma Prieta, California earthquake. *Geophysical Research Letters*, *17*(9), 1441-1444

300    Michael, A. J. (1991). Spatial variations in stress within the 1987 Whittier Narrows, California, aftershock

301          sequence: New techniques and results. *Journal of Geophysical Research: Solid Earth*, *96*(B4), 6303-

302          6319.

303    McKenzie, D. P. (1969). The relation between fault plane solutions for earthquakes and the directions of the

304           principal stresses. *Bulletin of the Seismological Society of America*, *59*(2), 591-601.

305    Medina, F. (2008). Catalogue of focal mechanisms of Moroccan earthquakes for the period 1959-2007. ISBN:

306           9954-8347-9-6 http://www.israbat.ac.ma/wp-content/uploads/2015/03/03-

307           %20Medina%20et%20al.%20(19-30).pdf

308    Peláez, J.A., M. Chourak, B. A. Tadili, L. Aït Brahim, M. Hamdache, C. López Casado, J. M. Martínez Solares;

309           A Catalog of Main Moroccan Earthquakes from 1045 to 2005. *Seismological Research Letters*2007;; 78

310           (6): 614–621. doi: https://doi.org/10.1785/gssrl.78.6.614

311    Simpson, R.W. (1997) Quantifying Anderson's faulting types. BSSA 102(B8).

312    Townend, J., & Zoback, M. D. (2004). Regional tectonic stress near the San Andreas fault in central and southern

313           California. *Geophysical Research Letters*, *31*(15).

314    Varryčuk, V. Iterative joint inversion for stress and fault orientations from focal mechanisms. Geophys. J. Int.

315           199, 69–77 (2014).

316    Walsh, F. R. III, & Zoback, M. D. (2016). Probabilistic assessment of potential fault slip related to injection-

317           induced earthquakes: Application to north-central Oklahoma, USA. Geology, 44(12), 991–994.

318           https://doi.org/10.1130/G38275.1

319    Zoback, M. D. (2010). Reservoir geomechanics. New York: Cambridge University Press.

320    Zoback, M.L., First and second-order patterns of stress in the lithosphere: The world stress map project, Jour.

321           Geophys Res., 97, 11,703-11,728, 1992.

322

323

324

325

## Supporting Information

| | Model | Weighting | Friction | N | Aφ | Aφ std | SHmax | SHmax std | Mean misfit | Mean dCFS | Oukaimedene misfit | Oukaimedene dCFS | Oukaimedene aux misfit | Oukaimedene aux dCFS | |
|---|---|---|---|---|---|---|---|---|---|---|---|---|---|---|---|
| All mechanisms | 0 | Inverse distance | 0.3–0.9 | 28 | 2.16 | 0.14 | 177 | 4 | 24.6 | 4.8 | 5.4 | 5.8 | 21.9 | 27.7 | |
| Exclude Middle Atlas and Eastern High Atlas | 1 | Inverse distance | 0.3–0.9 | 21 | 2.07 | 0.15 | 2 | 5 | 25.5 | 2.8 | 1.7 | 3.6 | 31.6 | 21.9 | Preferred model |
| All mechanisms | 2 | Uniform | 0.3–0.9 | 28 | 2.11 | 0.1 | 162 | 2 | 25.6 | 4.4 | 9.6 | 10.8 | 39.9 | 26.3 | |
| Exclude Middle Atlas and Eastern High Atlas | 3 | Uniform | 0.3–0.9 | 21 | 2.19 | 0.13 | 168 | 4 | 26.8 | 3.3 | 2.4 | 4.3 | 24.4 | 25.6 | |
| Low friction (all mechanisms) | 4 | Uniform | 0.2–0.4 | 28 | 2.1 | 0.12 | 162 | 2 | 25.4 | 3 | 9.7 | 8.4 | 43.5 | 12.6 | |
| Low friction (exclude Middle Atlas and Eastern High Atlas) | 5 | Inverse distance | 0.2–0.4 | 21 | 1.92 | 0.17 | 3 | 5 | 23.4 | 2.2 | 0.6 | 4.6 | 36.5 | 9.5 | |
| SW planes only (all mechanisms) | 6 | Uniform | 0.3–0.9 | 28 | 2.3 | 0.15 | 166 | 2 | 32.5 | 17.3 | NaN | NaN | 27.2 | 35.1 | |
| SW planes only (exclude Middle Atlas and Eastern High Atlas) | 7 | Inverse distance | 0.3–0.9 | 21 | 1.67 | 0.23 | 0 | 3 | 36.3 | 15.2 | NaN | NaN | 23.3 | 25.6 | |
| SW planes only, low friction (exclude Middle Atlas and Eastern High Atlas) | 8 | Inverse distance | 0.2–0.4 | 21 | 1.67 | 0.24 | 0 | 3 | 36.4 | 13.2 | NaN | NaN | 23.7 | 21.8 | |
| Southern High/Middle Atlas junction, Central and Western High Atlas | 9 | Inverse distance | 0.3–0.9 | 15 | 1.85 | 0.16 | 2 | 6 | 20.3 | 3.2 | 8 | 6.1 | 36.6 | 18.9 | Too few mechanisms for reliable inversion |
| Central and Western High Atlas only | 10 | Inverse distance | 0.3–0.9 | 10 | 1.75 | 0.18 | 5 | 7 | 15.6 | 2.4 | 11.1 | 10.3 | 43.8 | 16.7 | Too few mechanisms for reliable inversion |
| Western High Atlas only | 11 | Inverse distance | 0.3–0.9 | 6 | 1.59 | 0.24 | 9 | 10 | 7.4 | 3.5 | 17.5 | 9.5 | 39.6 | 7.5 | Too few mechanisms for reliable inversion |

**Table S1: Summary of alternative models**

| ID | Longitude | Latitude | Depth | Strike, Model 0 | Dip, Model 0 | Rake, Model 0 | Aux Strike, Model 0 | Aux Dip, Model 0 | Aux Rake, Model 0 | Misfit Mech 1, Model 0 | dCFS Plane 1, Model 0 | Misfit Mech 2, Model 0 | dCFS Plane 2, Model 0 | Strike, Model 1 | Dip, Model 1 | Rake, Model 1 | Misfit Mech 1, Model 1 | dCFS, Model 1 |
|----|-----------|----------|-------|-----------------|--------------|---------------|---------------------|------------------|-------------------|------------------------|-----------------------|------------------------|-----------------------|-----------------|--------------|---------------|------------------------|---------------|
| 1 | -5.97 | 31.92 | 10 | 314.23 | 63.935 | -134.31 | 200 | 50 | -35 | 56.2022 | 2.58496 | 58.385 | 2.03365 | 200 | 50 | -35 | 50.5522 | 4.0878 |
| 2 | -5.75 | 32.16 | 11 | 87.376 | 28.905 | 119.03 | 235 | 65 | 75 | 6.8091 | 3.04708 | 43.322 | 9.97962 | 87.3756 | 28.905 | 119.03 | 14.7903 | 2.3641 |
| 3 | -6.07 | 32.36 | 11 | 114.11 | 41.41 | 130.89 | 245 | 60 | 60 | 5.18833 | 0.51804 | 14.057 | 15.4355 | 114.107 | 41.41 | 130.89 | 8.42132 | 0.6155 |
| 4 | -4.91 | 32.56 | 12 | 225 | 50 | 50 | 97.546 | 54.068 | 127.45 | 15.0249 | 1.28515 | 15.893 | 3.94088 | 225 | 50 | 50 | 22.3992 | 0.9 |
| 5 | -5.78 | 31.95 | 12 | 35.12 | 80.038 | -5.0767 | 126 | 85 | -170 | 18.7206 | 0.30084 | 43.411 | 6.51484 | 35.1196 | 80.038 | -5.0767 | 13.7767 | 0.4053 |
| 6 | -7.29 | 31.33 | 16 | 339.97 | 69.746 | -142.31 | 235 | 55 | -25 | 22.4364 | 4.00881 | 65.026 | 6.16172 | 339.974 | 69.746 | -142.31 | 26.187 | 1.0519 |
| 7 | -7.32 | 31.34 | 13 | 135 | 90 | 145 | 225 | 55 | 0 | 7.24668 | 3.32386 | 32.722 | 1.95398 | 135 | 90 | 145 | 11.3668 | 4.6338 |
| 8 | -5.53 | 32.34 | 8.4 | 35 | 52 | 90 | 215 | 38 | 90 | 37.1972 | 5.01617 | 59.7 | 0.11337 | 35 | 52 | 90 | 50.1748 | 4.1086 |
| 9 | -6.26 | 32.24 | 9.1 | 68.871 | 30.539 | 100.26 | 237 | 60 | 84 | 3.03136 | 5.29478 | 45.973 | 9.74043 | 68.8712 | 30.539 | 100.26 | 12.7965 | 3.7293 |
| 10 | -5.39 | 32.39 | 7.6 | 32 | 63 | 90 | 212 | 27 | 90 | 54.5373 | 2.38623 | 64.015 | 0.63848 | 32 | 63 | 90 | 65.8298 | 2.2406 |
| 11 | -5.38 | 32.43 | 5.9 | 70 | 25 | 90 | 250 | 65 | 90 | 15.0086 | 7.02912 | 43.108 | 23.8485 | 70 | 25 | 90 | 5.23347 | 6.2119 |
| 12 | -5.34 | 32.41 | 13.7 | 28 | 58 | 90 | 208 | 32 | 90 | 49.9457 | 5.90369 | 65.639 | 0.33333 | 28 | 58 | 90 | 62.9227 | 4.6643 |
| 13 | -6.2 | 32.45 | 5.2 | 30 | 50 | 90 | 210 | 40 | 90 | 36.7687 | 7.42957 | 62.932 | 0.23738 | 30 | 50 | 90 | 50.3065 | 6.1674 |
| 14 | -6.18 | 32.24 | 5.5 | 45 | 50 | 90 | 225 | 40 | 90 | 27.966 | 2.75384 | 52.389 | 0.09726 | 45 | 50 | 90 | 40.322 | 2.379 |
| 15 | -5.6 | 32.38 | 6.4 | 30 | 55 | 90 | 210 | 35 | 90 | 44.2433 | 5.81278 | 63.501 | 0.1136 | 30 | 55 | 90 | 57.4407 | 4.732 |
| 16 | -6.06 | 31.49 | 33 | 20.732 | 76.115 | 22.699 | 285 | 68 | 165 | 16.5516 | 4.98161 | 21.345 | 26.9387 | 20.7319 | 76.115 | 22.699 | 24.0146 | 4.3327 |
| 17 | -9.62 | 31.35 | 25 | 322.93 | 79.169 | -169.82 | 231 | 80 | -11 | 7.36412 | 1.09044 | 20.389 | 9.54836 | 322.933 | 79.169 | -169.82 | 2.77343 | 1.3693 |
| 18 | -9.73 | 30.41 | 0.2 | 141.55 | 67.22 | 139.25 | 250 | 53 | 29 | 1.26877 | 0.41315 | 27.987 | 13.4644 | 141.552 | 67.22 | 139.25 | 3.89291 | 0.957 |
| 19 | -5.78 | 32 | 23 | 212 | 42 | 16 | 109.97 | 79.372 | 130.88 | 12.3224 | 0.19055 | 1.9433 | 15.2311 | 212 | 42 | 16 | 4.52589 | 0.6468 |
| 20 | -8.391 | 31.064 | 26 | 121.97 | 29.358 | 133.03 | 255 | 69 | 69 | 5.32089 | 5.21584 | 19.815 | 32.0415 | 121.967 | 29.358 | 133.03 | 1.70956 | 3.6102 |
| 21 | -9.6 | 30.5 | 0 | 44 | 90 | 10 | 314 | 80 | 180 | 5.08449 | 2.87071 | 15.486 | 3.68374 | 44 | 90 | 10 | 6.53682 | 0.8038 |
| 22 | -5.19 | 32.89 | 7 | 190 | 48 | 44 | 67.131 | 58.92 | 128.62 | 21.4968 | 7.24842 | 52.119 | 6.20367 | NaN | NaN | NaN | NaN | NaN |
| 23 | -5.25 | 33.17 | 10 | 203.5 | 67.5 | 11 | 109.25 | 79.847 | 157.12 | 10.0357 | 2.02102 | 24.476 | 16.0907 | NaN | NaN | NaN | NaN | NaN |
| 24 | -5.16 | 33.18 | 7 | 334.04 | 44.125 | -158.18 | 228 | 75 | -48 | 49.39 | 3.25653 | 64.546 | 6.92859 | NaN | NaN | NaN | NaN | NaN |
| 25 | -5.28 | 33.4 | 12 | 314.02 | 47.933 | -139.23 | 194 | 61 | -50 | 76.4602 | 2.27383 | 74.613 | 5.62258 | NaN | NaN | NaN | NaN | NaN |
| 26 | -4.32 | 31.29 | 5.4 | 187 | 69 | 12 | 92.644 | 78.808 | 158.57 | 19.9153 | 12.0207 | 48.241 | 26.0603 | NaN | NaN | NaN | NaN | NaN |
| 27 | -4.38 | 31.24 | 8 | 181 | 87 | 18 | 90.026 | 72.026 | 176.85 | 34.7788 | 20.3606 | 72.682 | 19.5246 | NaN | NaN | NaN | NaN | NaN |
| 28 | -4.08 | 32.6 | 23 | 182 | 71 | 7 | 89.711 | 83.383 | 160.87 | 36.1615 | 17.3809 | 54.449 | 32.1086 | NaN | NaN | NaN | NaN | NaN |

**Table S2: Focal mechanisms**
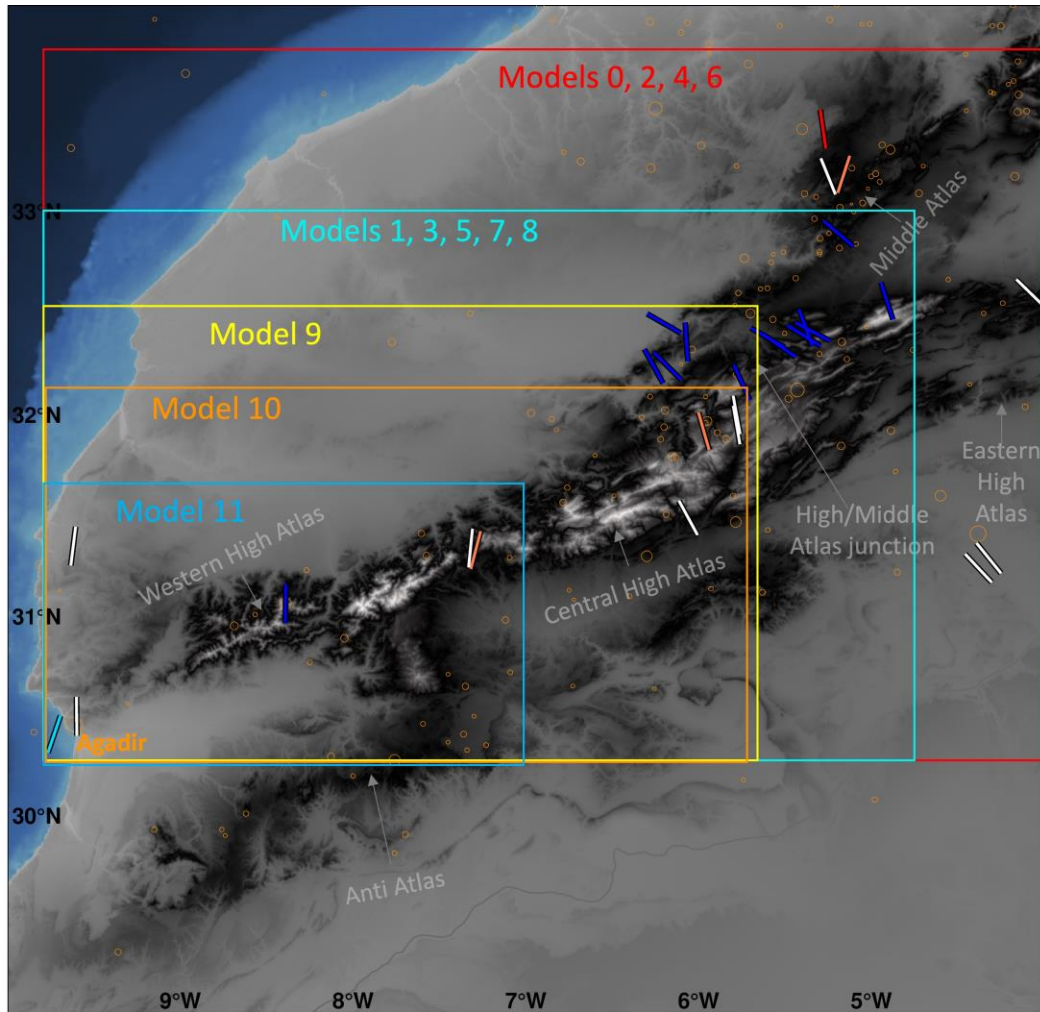
**Figure S1: Extents of the 11 models examined.** Models 9, 10, and 11 include fewer than 20 focal mechanisms so should not be considered reliable.

## Model 5: Low-friction faults

**Stress Inversion Results:**
**Low friction (0.2–0.4)**

$A\phi=1.92\pm0.17$
$\sigma_{Hmax}$ N3E$\pm5°$
$n=21$
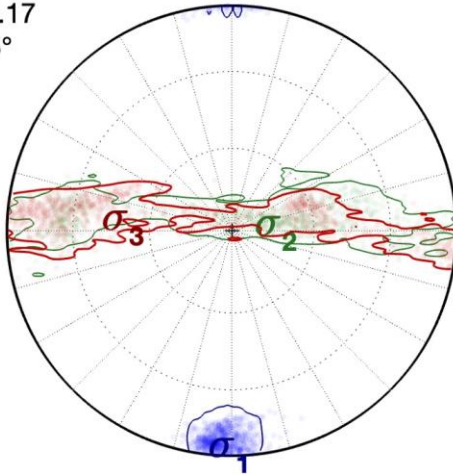
**Fault slip potential:**
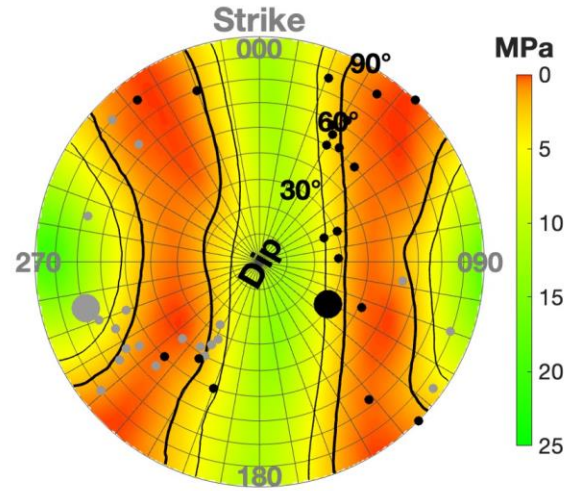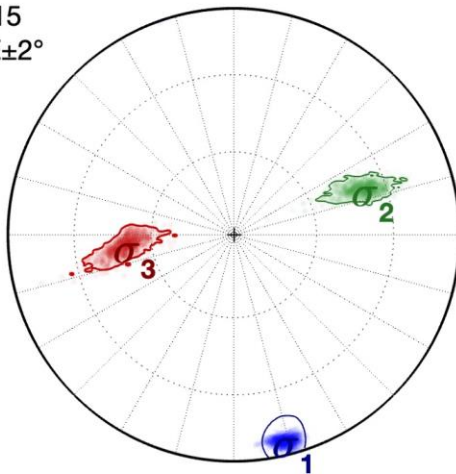**Low friction (0.2–0.4)**

339

340    **Figure S2: Low-friction faults** Inversion scheme is the same as Model 1 except a random friction 0.2–0.4 is selected for each
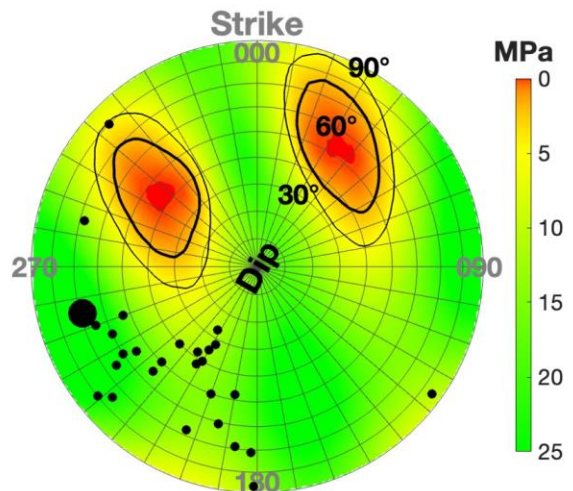
341    of 1001 inversions and FSP models.

342

343

## Model 6: SW-striking planes only

**Stress inversion results:**

$A\phi=2.3\pm0.15$
$\sigma_{Hmax}$ N166E$\pm2°$
$n=28$

**Fault slip potential:**

344

345 **Figure S3: SW-striking focal planes** For each event, the more southwesterly nodal plane is set as the focal plane.

346



Model 8: SW-striking planes only & low friction faults
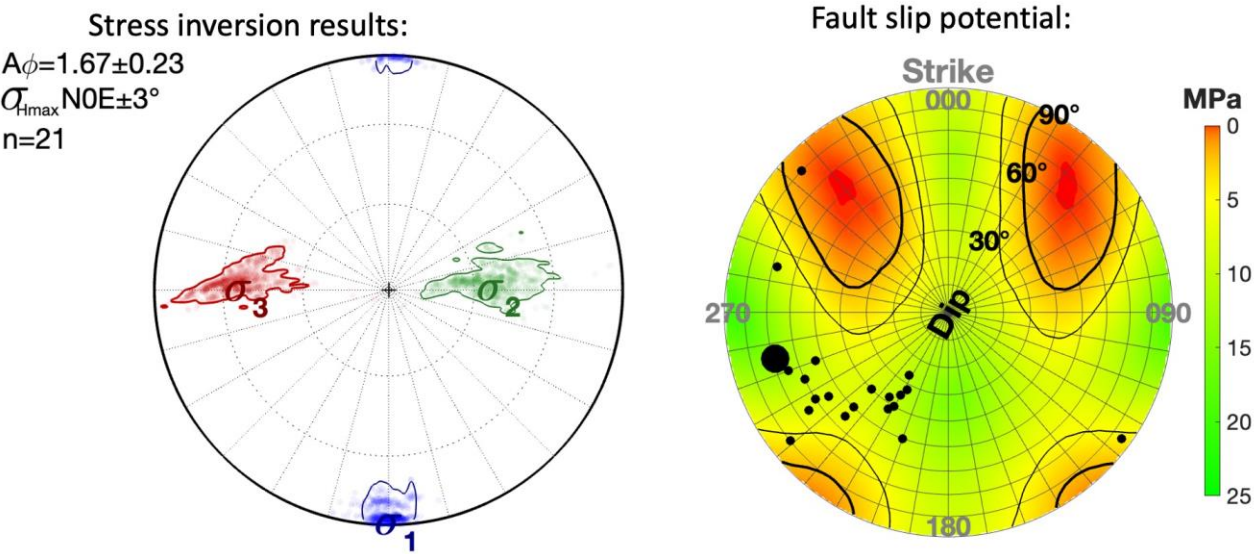
347

348 **Figure S4: SW-striking focal planes with low friction.** For each event, the more southwesterly nodal plane is set as the

349 focal plane. This model also differs from Model 6 (Figure S2) in excluding events from the Middle Atlas and Eastern High

350 Atlas, and in weighting the retained mechanisms by inverse-distance from Oukaïmedene (instead of uniform weights).

351
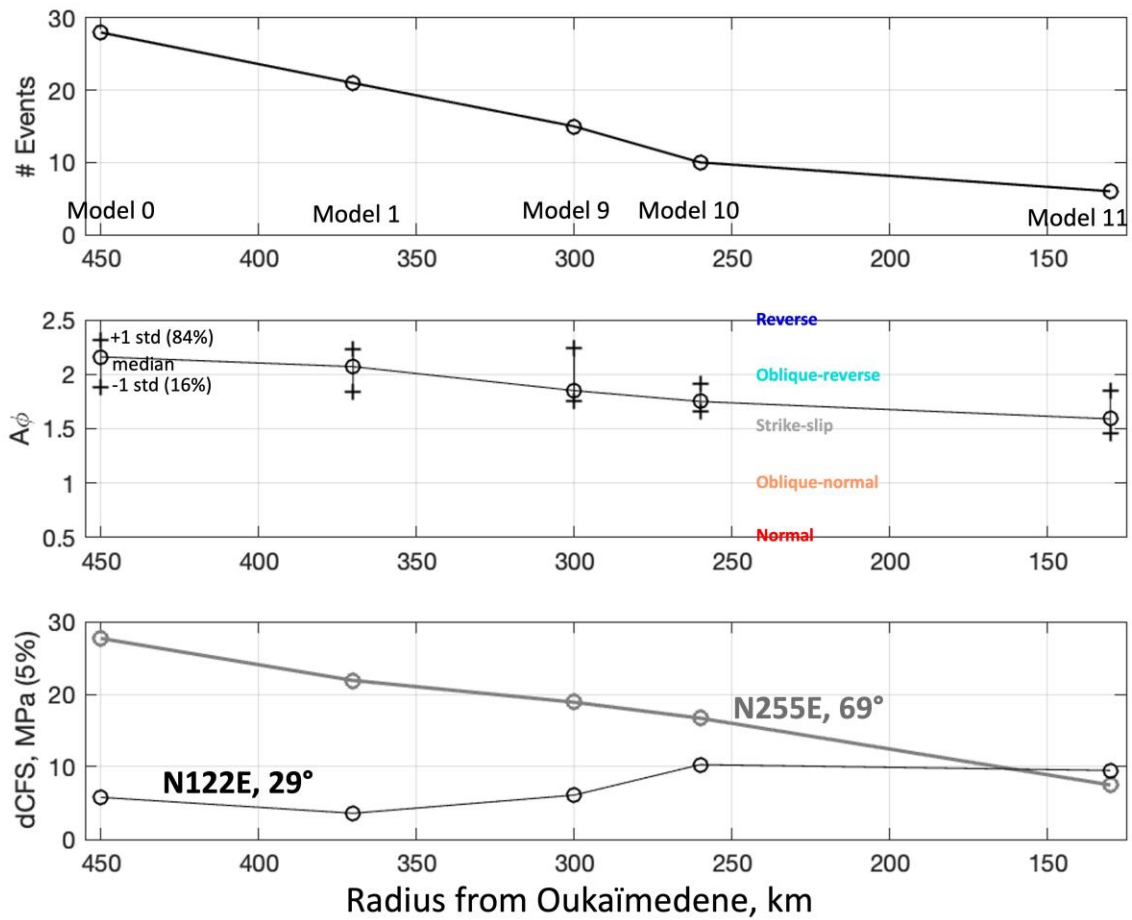
**Figure S6: Inversions with fewer mechanisms.** The area from which focal mechanisms are gathered narrows in on the

Western High Atlas from left to right. (**Top**) The number of focal mechanisms decreases. The associated models are indicated.

(**Middle**) Aϕ decreases, suggesting a transition from characteristically reverse-oblique faulting to strike-slip. Circles denote the

median across 1001 inversions; crosses delineate the 16%–84% confidence interval (±1 standard deviation for normal

distributions). (**Bottom**) The WSW-striking nodal plane becomes progressively better aligned for slip and appears to be as well

oriented as the ESE-striking plane when only the Western High Atlas is considered (Model 11). Models 9, 10, and 11 use too

few focal mechanisms to provide robust results, however.

359

360

| ID | Longitude | Latitude | Depth | Strike, Model 0 | Dip, Model 0 | Rake, Model 0 | Aux Strike, Model 0 | Aux Dip, Model 0 | Aux Rake, Model 0 |
|----|-----------|----------|-------|-----------------|--------------|---------------|---------------------|------------------|-------------------|
| 1 | -5.97 | 31.92 | 10 | 314.23 | 63.935 | -134.31 | 200 | 50 | -35 |
| 2 | -5.75 | 32.16 | 11 | 87.376 | 28.905 | 119.03 | 235 | 65 | 75 |
| 3 | -6.07 | 32.36 | 11 | 114.11 | 41.41 | 130.89 | 245 | 60 | 60 |
| 4 | -4.91 | 32.56 | 12 | 225 | 50 | 50 | 97.546 | 54.068 | 127.45 |
| 5 | -5.78 | 31.95 | 12 | 35.12 | 80.038 | -5.0767 | 126 | 85 | -170 |
| 6 | -7.29 | 31.33 | 16 | 339.97 | 69.746 | -142.31 | 235 | 55 | -25 |
| 7 | -7.32 | 31.34 | 13 | 135 | 90 | 145 | 225 | 55 | 0 |
| 8 | -5.53 | 32.34 | 8.4 | 35 | 52 | 90 | 215 | 38 | 90 |
| 9 | -6.26 | 32.24 | 9.1 | 68.871 | 30.539 | 100.26 | 237 | 60 | 84 |
| 10 | -5.39 | 32.39 | 7.6 | 32 | 63 | 90 | 212 | 27 | 90 |
| 11 | -5.38 | 32.43 | 5.9 | 70 | 25 | 90 | 250 | 65 | 90 |
| 12 | -5.34 | 32.41 | 13.7 | 28 | 58 | 90 | 208 | 32 | 90 |
| 13 | -6.2 | 32.45 | 5.2 | 30 | 50 | 90 | 210 | 40 | 90 |
| 14 | -6.18 | 32.24 | 5.5 | 45 | 50 | 90 | 225 | 40 | 90 |
| 15 | -5.6 | 32.38 | 6.4 | 30 | 55 | 90 | 210 | 35 | 90 |
| 16 | -6.06 | 31.49 | 33 | 20.732 | 76.115 | 22.699 | 285 | 68 | 165 |
| 17 | -9.62 | 31.35 | 25 | 322.93 | 79.169 | -169.82 | 231 | 80 | -11 |
| 18 | -9.73 | 30.41 | 0.2 | 141.55 | 67.22 | 139.25 | 250 | 53 | 29 |
| 19 | -5.78 | 32 | 23 | 212 | 42 | 16 | 109.97 | 79.372 | 130.88 |
| 20 | -8.391 | 31.064 | 26 | 121.97 | 29.358 | 133.03 | 255 | 69 | 69 |
| 21 | -9.6 | 30.5 | 0 | 44 | 90 | 10 | 314 | 80 | 180 |
| 22 | -5.19 | 32.89 | 7 | 190 | 48 | 44 | 67.131 | 58.92 | 128.62 |
| 23 | -5.25 | 33.17 | 10 | 203.5 | 67.5 | 11 | 109.25 | 79.847 | 157.12 |
| 24 | -5.16 | 33.18 | 7 | 334.04 | 44.125 | -158.18 | 228 | 75 | -48 |
| 25 | -5.28 | 33.4 | 12 | 314.02 | 47.933 | -139.23 | 194 | 61 | -50 |
| 26 | -4.32 | 31.29 | 5.4 | 187 | 69 | 12 | 92.644 | 78.808 | 158.57 |
| 27 | -4.38 | 31.24 | 8 | 181 | 87 | 18 | 90.026 | 72.026 | 176.85 |
| 28 | -4.08 | 32.6 | 23 | 182 | 71 | 7 | 89.711 | 83.383 | 160.87 |

| Misfit Mech 1, Model 0 | dCFS Plane 1, Model 0 | Misfit Mech 2, Model 0 | dCFS Plane 2, Model 0 | Strike, Model 1 | Dip, Model 1 | Rake, Model 1 | Misfit Mech 1, Model 1 | dCFS, Model 1 |
|---|---|---|---|---|---|---|---|---|
| 56.2022 | 2.58496 | 58.385 | 2.03365 | 200 | 50 | -35 | 50.5522 | 4.0878 |
| 6.8091 | 3.04708 | 43.322 | 9.97962 | 87.3756 | 28.905 | 119.032 | 14.7903 | 2.3641 |
| 5.18833 | 0.51804 | 14.057 | 15.4355 | 114.107 | 41.41 | 130.893 | 8.42132 | 0.6155 |
| 15.0249 | 1.28515 | 15.893 | 3.94088 | 225 | 50 | 50 | 22.3992 | 0.9 |
| 18.7206 | 0.30084 | 43.411 | 6.51484 | 35.1196 | 80.038 | -5.0767 | 13.7767 | 0.4053 |
| 22.4364 | 4.00881 | 65.026 | 6.16172 | 339.974 | 69.746 | -142.31 | 26.187 | 1.0519 |
| 7.24668 | 3.32386 | 32.722 | 1.95398 | 135 | 90 | 145 | 11.3668 | 4.6338 |
| 37.1972 | 5.01617 | 59.7 | 0.11337 | 35 | 52 | 90 | 50.1748 | 4.1086 |
| 3.03136 | 5.29478 | 45.973 | 9.74043 | 68.8712 | 30.539 | 100.262 | 12.7965 | 3.7293 |
| 54.5373 | 2.38623 | 64.015 | 0.63848 | 32 | 63 | 90 | 65.8298 | 2.2406 |
| 15.0086 | 7.02912 | 43.108 | 23.8485 | 70 | 25 | 90 | 5.23347 | 6.2119 |
| 49.9457 | 5.90369 | 65.639 | 0.33333 | 28 | 58 | 90 | 62.9227 | 4.6643 |
| 36.7687 | 7.42957 | 62.932 | 0.23738 | 30 | 50 | 90 | 50.3065 | 6.1674 |
| 27.966 | 2.75384 | 52.389 | 0.09726 | 45 | 50 | 90 | 40.322 | 2.379 |
| 44.2433 | 5.81278 | 63.501 | 0.1136 | 30 | 55 | 90 | 57.4407 | 4.732 |
| 16.5516 | 4.98161 | 21.345 | 26.9387 | 20.7319 | 76.115 | 22.6985 | 24.0146 | 4.3327 |
| 7.36412 | 1.09044 | 20.389 | 9.54836 | 322.933 | 79.169 | -169.82 | 2.77343 | 1.3693 |
| 1.26877 | 0.41315 | 27.987 | 13.4644 | 141.552 | 67.22 | 139.253 | 3.89291 | 0.957 |
| 12.3224 | 0.19055 | 1.9433 | 15.2311 | 212 | 42 | 16 | 4.52589 | 0.6468 |
| 5.32089 | 5.21584 | 19.815 | 32.0415 | 121.967 | 29.358 | 133.033 | 1.70956 | 3.6102 |
| 5.08449 | 2.87071 | 15.486 | 3.68374 | 44 | 90 | 10 | 6.53682 | 0.8038 |
| 21.4968 | 7.24842 | 52.119 | 6.20367 | NaN | NaN | NaN | NaN | NaN |
| 10.0357 | 2.02102 | 24.476 | 16.0907 | NaN | NaN | NaN | NaN | NaN |
| 49.39 | 3.25653 | 64.546 | 6.92859 | NaN | NaN | NaN | NaN | NaN |
| 76.4602 | 2.27383 | 74.613 | 5.62258 | NaN | NaN | NaN | NaN | NaN |
| 19.9153 | 12.0207 | 48.241 | 26.0603 | NaN | NaN | NaN | NaN | NaN |
| 34.7788 | 20.3606 | 72.682 | 19.5246 | NaN | NaN | NaN | NaN | NaN |
| 36.1615 | 17.3809 | 54.449 | 32.1086 | NaN | NaN | NaN | NaN | NaN |

El Moudnib et al., 2023 Event 1 2009 07 06
El Moudnib et al., 2023 Event 2 2010 08 05
El Moudnib et al., 2023 Event 3 2010 08 05 doublet?  Martin et al. (2015) 53 36 82 243 54 96
El Moudnib et al., 2023 Event 4 2011 05 01
El Moudnib et al., 2023 Event 5 2011 02 14 Martin et al. (2015) 38 84 -4 129 85 -174
El Moudnib et al., 2023 Event 6 2011-12-26
El Moudnib et al., 2023 Event 7 2011-12-26 duplicate or doublet?
El Moudnib et al., 2023 Event 8 2013 04 27
El Moudnib et al., 2023 Event 9 2013 05 27
El Moudnib et al., 2023 Event 10 2013 05 31
El Moudnib et al., 2023 Event 11 2013 05 31
El Moudnib et al., 2023 Event 12 2013 06 25
El Moudnib et al., 2023 Event 13 2014 03 12
El Moudnib et al., 2023 Event 14 2014 05 12
El Moudnib et al., 2023 Event 15 2014 05
1967 08 28 21 15 36  see Medina, 2008 - hybrid solution using Medina & Cherakaoui 1992 and
1988 12 16 22 34 41
1992 04 05 21 16 38
global CMT 012886C
Oukaïmedene 2023 09 08 22 11 02 from USGS
1960 02 29 Agadir event from Hatzfeld: Other solutions (Medina, 2008) have aberrant E–W sho
1979 06 16 13 51 43 Medina (2008)
2007 08 11 20 46 PondrelliRCMT - World Stress Map
1979 01 21 08 06 06 Medina (2008)
1979 01 17 17 43 33 Medina (2008)
1992 10 23  gCMT / Medina (2008)
1992 10 30 0 43 55 gCMT / Medina
gCMT 201911170839A

Moreira 1986

ortening